

Ferrofluidic Manipulator: Automatic Manipulation of Non-magnetic Microparticles at Air-Ferrofluid Interface

Zoran Cenev[†], P.A. Diluka Harischandra[†], Seppo Nurmi, Mika Latikka, Ville Hynninen, Robin H. A. Ras, Jaakko V. I. Timonen and Quan Zhou^{*}

Abstract— Manipulation of small-scale matter is a fundamental topic in micro- and nanorobotics. Numerous magnetic robotic systems have been developed for the manipulation of microparticles in an ambient environment, liquid as well as on the air-liquid interface. Those systems move intrinsically magnetic or magnetically tagged objects by inducing a magnetic torque or force. However, most of the materials found in nature are non-magnetic. Here, we report a novel ferrofluidic manipulator for automatic two-dimensional manipulation of non-magnetic objects floating on top of a ferrofluid. The manipulation system employs eight centimeter-scale solenoids, which can move non-magnetic particles floating on the air-liquid interface by deforming the air-ferrofluid interface. Using linear programming, we can control the motion of non-magnetic particles with a predefined trajectory of a line, square, and circle with a precision of $57.4 \pm 33.6 \mu\text{m}$, $74 \pm 44.4 \mu\text{m}$ and $67.2 \pm 38.6 \mu\text{m}$, respectively. The ferrofluidic manipulator is versatile with the materials and the shapes of the objects under manipulation. We have successfully manipulated particles made of polyethylene, polystyrene, a silicon chip, and poppy and sesame seeds.

Index Terms—soft robotics systems, smart material-based devices, micro-electro-mechanical systems.

I. INTRODUCTION

MAGNETIC field-driven manipulation of miniaturized robotic agents has attracted great research attention with a wide range of applications. Impressive results have been achieved during the last two decades ranging from contactless ocular surgery [1], targeted drug delivery [2], in-vitro diagnosis [3], endoscopy [4], minimally invasive surgery [5], and environmental remediation [6] to name a few. Magnetic fields have been widely utilized in robotic micromanipulation due to their transparency to human and animal tissues, and their capacity to wirelessly address micro-objects. It has been shown that magnetic-driven microrobotic systems are capable of

performing independent control of multiple magnetic agents in 2D [7] and 3D [8], selective manipulation and extraction [9], [10], motion and patterning of swarms [11], [12], as well as carrying out targeted gene delivery [13] and climbing on liquid menisci [14], among a remaining plethora of other reported capabilities [15]–[19].

However, most of the magnetic field-driven manipulation methods require that the object under manipulation features paramagnetic or ferromagnetic properties. To manipulate non-magnetic objects, magnetic tools are employed including magnetic pushers [20], [21], grippers [22], and magnetic agent-induced fluid flow [23]. Magnetic spray has also been used for magnetic tagging non-magnetic objects to enable magnetic manipulation [24].

Recently, magnetic liquids such as paramagnetic solutions and ferrofluids have found applications in microrobotics. For example, ferrofluidic droplets can act as shape-programmable magnetic miniature soft robots for splitting, regeneration, and navigation through small channels [25], [26]. The shape of magnetic liquids can be altered by an external magnetic field. Lately, we have discovered the underlying physical mechanism of displacing and trapping micro- and millimeter-sized non-magnetic particles at the air-paramagnetic liquid interface [27]. We have also shown that non-magnetic particles can be trapped and dragged at the air-paramagnetic liquid interface.

Here we propose a novel ferrofluidic manipulator that can automatically manipulate non-magnetic objects by controlling the curvature of air-ferrofluid interface using eight solenoids. The ferrofluidic manipulator can manipulate non-magnetic particles along predefined trajectories. The remaining part of the paper is structured as follows: Section II describes the working principle and the mechatronic design of the manipulator. Section III reports the properties of the centimeter-scale solenoids, the ferrofluid, as well as the manipulation

This work was supported in part by the Academy of Finland (projects #295006 and #317018).

[†]Zoran Cenev and P. A. Diluka Harischandra are co-first authors and have contributed equally to this work.

^{*}Corresponding author: quan.zhou@aalto.fi

Zoran Cenev, P.A. Diluka Harischandra and Quan Zhou are with Department of Electrical Engineering and Automation, School of Electrical Engineering, Aalto University, Maarintie 8, 02150 Espoo, Finland, e-mail (zoran.cenev@aalto.fi, diluka.harischandra@aalto.fi and quan.zhou@aalto.fi). Seppo Nurmi is with Department of Mechanical Engineering, School of

Engineering, Aalto University, Otakaari 4 (K3), 02150 Espoo, Finland (e-mail: seppo.nurmi@aalto.fi).

Zoran Cenev, Mika Latikka, Ville Hynninen, Robin H. A. Ras and Jaakko V. I. Timonen are with Department of Applied Physics, School of Science, Aalto University, Puumiehenkuja 2, 02150 Espoo, Finland (e-mail: mika.latikka@aalto.fi; ville.hynninen@aalto.fi; robin.ras@aalto.fi; jaakko.timonen@aalto.fi).

Robin H. A. Ras is with Department of Bioproducts and Biosystems, Aalto University, P.O. Box 16000, 02150 Espoo, Finland

This article has supplementary downloadable multimedia material available.

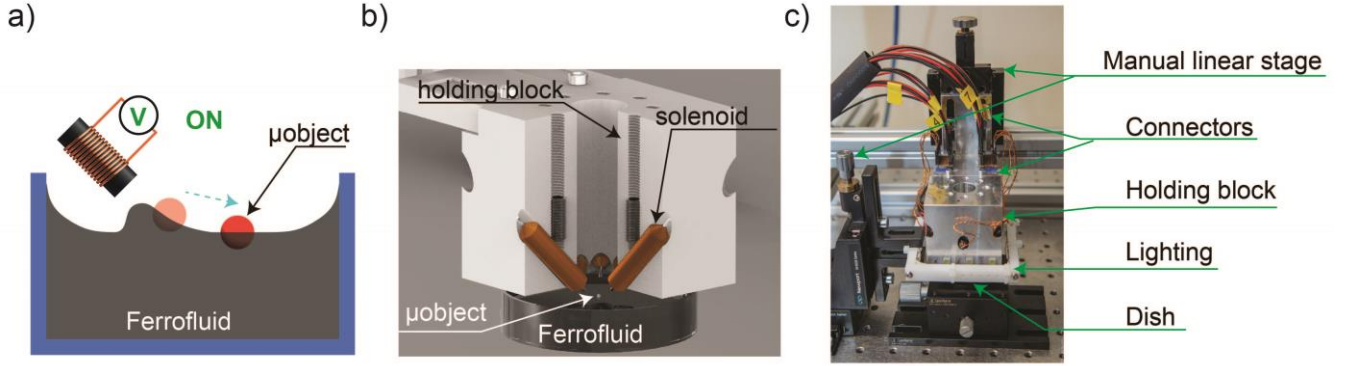


Fig. 1. Ferrofluid manipulator: the concept and interacting components for manipulating small-scale non-magnetic objects at the air-ferrofluid interface. Illustration not to scale. a) Concept of two-dimensional manipulation of a non-magnetic object: e.g. polyethylene particle b) Computer-aided design (CAD) rendered image of the mechanical assembly consisting of solenoids within a holding block located on top of a dish containing the ferrofluid and a particle at the air-ferrofluid interface. c) A photograph of the ferrofluidic manipulator showing the aluminum holder with the solenoids, a ring LED light, and a petri dish containing a ferrofluid sitting on a 2D goniometer stage. The manipulation platform resides on an anti-vibration table.

objects. The open-loop performance of the ferrofluidic manipulator is experimentally characterized and described in Section IV. Section V explains a path-following algorithm based on linear programming. Finally, Section VI discusses the results and concludes the paper.

II. SYSTEM OVERVIEW

A. Concept and working principle

Fig. 1a illustrates the manipulation concept of the ferrofluidic manipulator. A non-magnetic micro-object with a commensurate density to the one of the ferrofluid is placed on the air-ferrofluid interface. By applying a magnetic field to the air-magnetic liquid interface, the interface deforms into a bump and the particle is pushed away from the bump as well as from the source of the magnetic field as shown in Fig. 1a. The height of the bump is depending on the strength of magnetic field acting on the ferrofluidic surface, and in our manipulator, it is in the order of hundreds of micrometers. By superimposing the magnetic fields from different magnetic sources, micro- and millimeter-scale non-magnetic objects such as particles, chips, seeds can be manipulated in a desired trajectory.

The force acting on a micrometer-scaled object pinned at the air-magnetic liquid interface can be derived as a negative derivative ($F = -dE/d\rho$) from the total energy [27]:

$$E = E_0 + m_e g(u + l^2 H) - (\chi_L V_{imm} - \chi_p V_p) B^2 \frac{1}{\mu_0} \quad (1)$$

where E_0 is surface adsorption energy, m_e is the effective mass, g is gravitational acceleration, l is the capillary length of the magnetic liquid, ρ is distance along the horizontal axis for the polar coordinate system and $u(\rho)$ is the interface deformation caused by the magnetic field B , μ_0 is the permeability of free space, χ_L and χ_p are magnetic susceptibility of the liquid and the particle, respectively, and V_{imm} the immersion volume and V_p is the volume of the particle. The interface deformation $u(\rho)$ is obtained by applying the Green function which reads:

$$u(\rho) = \frac{1}{2\pi\gamma} \int_0^\infty dq q \int_0^{2\pi} K_0\left(\frac{|\vec{\rho} - \vec{q}|}{l}\right) \Pi(q) d\phi \quad (2)$$

and can be solved only numerically [27]. Here, γ is surface tension of the magnetic liquid, \vec{q} is the sweeping vector, ϕ the azimuthal angle between the two-dimensional vectors $\vec{\rho}$ and \vec{q} , K_0 is Bessel functions from the second kind and Π is the Maxwell tensor at the interface plane $z = 0$.

B. System components and mechatronic integration

Fig. 1b illustrates the computer-aided design of the mechanical assembly consisting of centimeter-scale solenoids within a holding block located on the top of a petri dish containing the ferrofluid and a particle at the air-ferrofluid interface. Fig. 1c, shows the major components and their implementation into one functional mechatronic system. The workspace is bounded by the solenoids in a circular arrangement with an offset of 45° from the horizontal plane and radially from each other as shown in Fig.1b. Manipulated objects are placed on the air-ferrofluid interface prior to any manipulation experiment. The manipulation workspace was imaged by a camera with a zoom macro lens placed on the top of the solenoids holding block providing visual information. The solenoids were controlled in a digital ON/OFF manner. The control signal was generated by a computer and transmitted to the custom-made electronic circuitry via a digital input/output board (NI DIO 6501, National Instruments, USA). The control software was written in C++ (Visual C++ version 16.0, Microsoft, USA).

1) Centimeter-scale solenoids

The solenoids have a ~ 4 cm metal core made of one-millimeter-thick martensitic stainless-steel wire (AISI 420), wrapped with copper wire (SWG 27, PKC Group, Finland) in 6 layers with 300 to 400 coil turns. Each coil has a resistance of $\sim 0.5 \Omega$ and inductance between 200 and 250 mH. The frontal end of each solenoid was grinded to be flat. The long solenoids had neck length of 4 to 6 mm and short solenoids of 1 to 2 mm.

The magnetic field intensity (Fig. 2a) of a short solenoid at 1.15 A excitation current was experimentally measured using a hall sensor (SS495A1, Honeywell Inc., USA). The magnetic

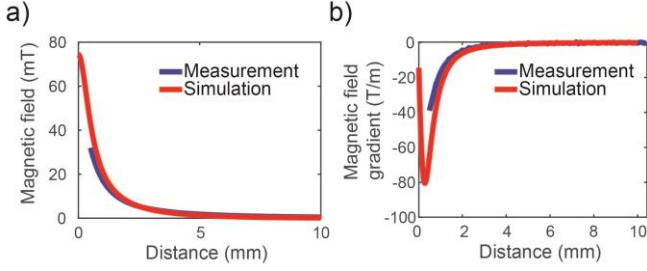


Fig. 2. Magnetic properties of a short solenoid when 1,15 A current (at a voltage rating of 5V) is running through it. **a)** Magnetic field intensity over distance and **b)** Magnetic field gradient over distance.

field gradient was numerically computed from the obtained data (Fig. 2b). The numerical simulation of the magnetic field and field gradient was also conducted in Comsol Multiphysics 5.2a (Comsol Group, Sweden). The measurements are in good agreement with the simulations.

In the numerical simulation, a 2D axisymmetric model was defined with geometry as close as possible to the real solenoid. A stationary magnetic field study was used to generate the magnetic fields (line, planar, and 3D data) and the field gradient. The data of the magnetic field and field gradient data was exported to MATLAB (MathWorks, USA) for plotting.

2) Mechanical Assembly

Eight solenoids were inserted into the aluminum holding block as shown in Fig. 1b. The solenoids were positioned along its centerline and eventually fixed by M4 headless hex screws. The tips of the solenoids are positioned in the range of 0.5-1 mm above the surface of the ferrofluid. The short and long solenoids were arranged alternately due to geometrical considerations. The resulting workspace, seen from a top view, is a circle with a diameter of up to about 8 mm. The holding block is mounted on a manual linear stage (Newport, USA) using connector pieces. The whole subassembly as such was mounted onto a frame made of 30 mm × 30 mm aluminum

profiles (Item, Germany).

3) Machine vision and video data acquisition

A camera (Point Gray GS3-U3-41C6C-C, Flir Systems Inc., Canada) with a magnification lens (Zoom Macro 7000, Navitar, USA) was mounted on top of the whole assembly to provide visual feedback of the manipulation. Image and video and data recording were performed using in-house developed software.

For the manipulation experiments of the particles and the seeds, the workspace was illuminated with a tailor-made rectangular frame with red-green-blue (RGB) light-emitting-diode (LED) light stripe (Velleman, Belgium) attached to a manual linear stage (Newport, USA). The LED stripe light source was placed between the aluminum holding block and the petri dish containing the ferrofluid.

C. Electronic circuitry

The solenoids were actuated by a custom-made electronic circuitry (Fig. 3). Each coil in the electronic circuitry is serially connected with a 3.3 Ω power resistor (Vishay, USA). The coil and the power resistor are in parallel connection with fly-back diode 1N4003 (Multicomp, Farnell, UK), where the cathode was facing the coil and the anode was facing the power resistor. Another parallel connection line consisting of 3 mm LED diode (Multicomp, Farnell, UK) and 330 Ω resistor (TE Connectivity, Switzerland) has been added for debugging purposes. The switching of a coil is arranged through a solid-state relay (Finder, Italy). This sub-circuitry has been used for each coil. The electric power was supplied through a laboratory power supply (DC E3634A, Keysight, USA). A 0.1 Ω shunt resistor with ≥ 3 W power rating (TT Electronics, UK) was installed on the ground (GND) line to monitor the current consumption of the circuitry. The relays were controlled by a digital input/output board (NI DIO 6501, National Instruments, USA) using 8 digital output channels. Each output channel was in parallel connection to a pull-up 4.7 KΩ resistor (TT Electronics,

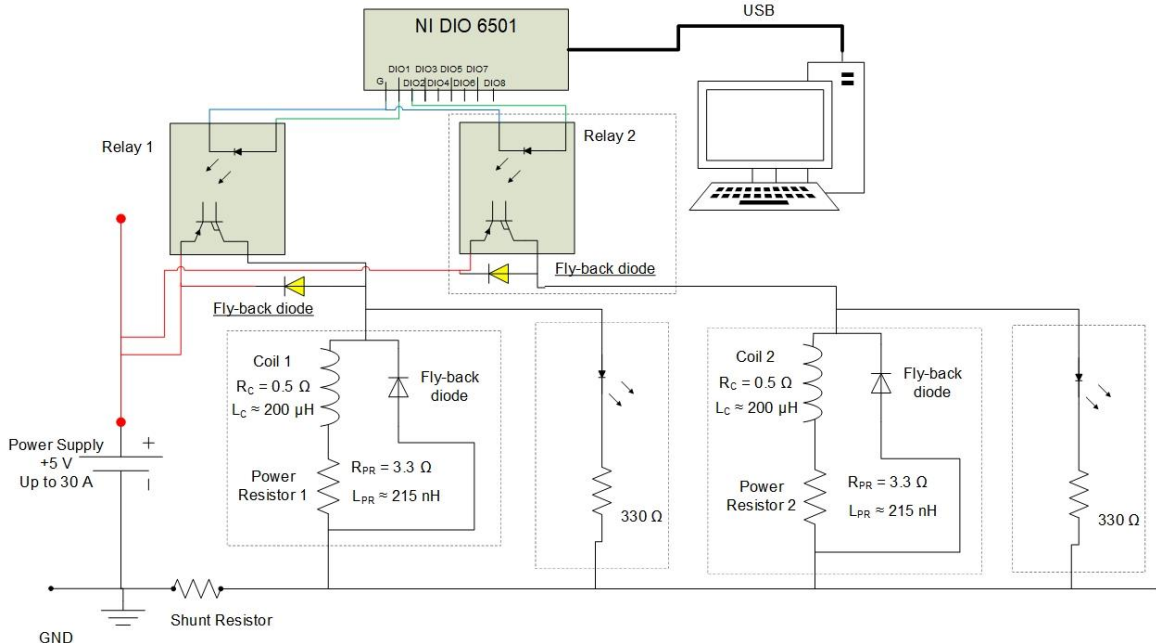


Fig. 3. Schematic of the custom-made electronic circuitry utilized in the ferrofluidic manipulator. Only two relays are illustrated. For simplification purposes, the following components are not illustrated: Pull-up resistors within the NI DIO 6501; LEDs and resistors for LEDs on the Relays' inputs.

UK). The overall resistance in one line in which a solenoid is actuated is $\sim 4.2 \Omega$ (3.3Ω from a solenoid, 0.5Ω from the power resistor, and 0.4Ω from resistance in the cables). The current-voltage dependency in each solenoid was heuristically identified to be linear for the range of voltages utilized for micro-object manipulation, for 2-6 V, with corresponding current of about 0.47 A – 1.4 A. Due to the minor variation of the resistances among different solenoids, the constant voltage from the power supply may lead to slightly different currents in each solenoid.

III. MATERIALS

A. Preparation of water-based ferrofluid

Water-based ferrofluid ($\text{FeCl}_3 @ \text{H}_2\text{O}$) was prepared through the coprecipitation method. 8.65 g of iron (III) chloride hexahydrate and 3.18 g of iron (II) chloride tetrahydrate were dissolved in 288 g of MQ water followed by coprecipitation through the addition of 32 ml of ammonium hydroxide (28 % – 30 %). The resulting black dispersion was stirred for 5 min after which 10.1 g of citric acid monohydrate was added to stabilize the particles followed by another 5 min of stirring. The particles were sedimented with a strong magnet, aqueous supernatant discarded by decantation, and then re-dispersed with an additional 1.86 g of citric acid monohydrate in 80 ml of MQ H_2O by stirring for 5 min. 160 ml of acetone was added, the dispersion was then magnetically decanted, and the particles were re-dispersed in 80 ml of MQ H_2O . This magnetic decantation washing cycle was repeated twice. After one more cycle of magnetic decantation, the particles were re-dispersed in MQ H_2O to obtain a water-based ferrofluid.

B. Characterization of the physical quantities of the utilized ferrofluid

The magnetic moment of the ferrofluids was measured in a multipurpose measurement system (PPMS Dynacool, Quantum Design, USA) using the Vibrating Sample Magnetometer (VSM) mode with a range from -1 to 1 T. Fig. 4 shows the magnetic characteristic of the ferrofluids used in our experimental work. One should note that the nanoparticle concentration of the water-based ferrofluid increased slowly with time due to evaporation, since the ferrofluid was reused in several experiments

The surface tension of a ferrofluid sample was measured by contact angle goniometer Attension® Theta (Biolin Scientific, Sweden). The viscosity of the ferrofluid was measured with

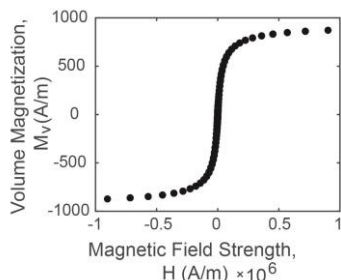


Fig. 4. Magnetic characteristics of a ferrofluid with a concentration of 12.4 mg/ml of iron (III) chloride in water as a carrier medium.

TABLE I. PROPERTIES OF THE UTILIZED FERROFLUID

Parameter	Value
Viscosity (mP·s)	0.9
Density (kg/m ³)	1071
Surface Tension (mN/m)	74.75 (± 0.15)
Evaporation (ml/h)	0.6

Physica MCR 300 (Anton Paar GmbH, Austria).

The evaporation rate was measured by observing the Petri dish (diameter: 55 mm) filled with ferrofluid and measuring its mass with a precision scale (EK-400H, A&D Company LTD, Japan) every 10 minutes for overall duration of 90 to 120 minutes per sample. The measured properties of the ferrofluid are summarized in Table I. The properties of the ferrofluid may have changes during the manipulation experiments due to evaporation and absorption when exposed to air.

C. Manipulation objects

For the manipulation experiments, different types of non-magnetic objects were used. The system is characterized using a 550 μm diameter polyethylene (PE) spherical particle (PE, Cospheric LLC, USA). Other manipulation objects used for the experiments include a 1 mm diameter polystyrene (PS) spherical particle (PSS-1.05, Cospheric LLC, USA) and a 980 $\mu\text{m} \times 980 \mu\text{m} \times 540 \mu\text{m}$ sized silicon chip. Additionally, poppy and sesame seeds were used for demonstrating the manipulation of biologically relevant matter.

IV. OPEN-LOOP PERFORMANCE

To examine the trajectory of particle motion under manipulation, a PE particle was placed about 2 mm in front of a short solenoid and then the solenoid was actuated with a constant current of 1.43 A. The resulted trajectories for two repetitions of the open-loop tests are shown in Fig. 5a, and see the Supplementary multimedia file for videos. The actuation of the solenoid pushes the particle to the center of the workspace and beyond in a slightly curved line attributed to the topology of the ferrofluid surface during manipulation. The motion of the particle is largely repeatable as shown in the figure. During the tests, the particle passed the center and much beyond, showing that the manipulator is capable of manipulating particles within the workspace enclosed by the tip of the solenoids.

To characterize the velocity of particle motion under manipulation, we calculate the mean velocity during the first second after actuation of an initially resting PE particle. The mean velocity during the first second, or actuation velocity hereafter, as a function of the particle-solenoid initial distance was experimentally studied. Fig. 5b depicts the mean and standard deviation of the actuation velocity of the actuated particles at five different initial distances (1.91 mm, 2.80 mm, 3.70 mm, 4.60 mm, 5.50 mm) at constant excitation current of 1.43 A, where the experiment was repeated five times for each distance. The actuation velocity was 0.58 ± 0.01 mm/s at 1.91 mm initial distance and monotonically decreasing in a linear fashion to 0.08 ± 0.05 mm/s at 5.50 mm initial distance, see the Supplementary multimedia file for videos. This negative

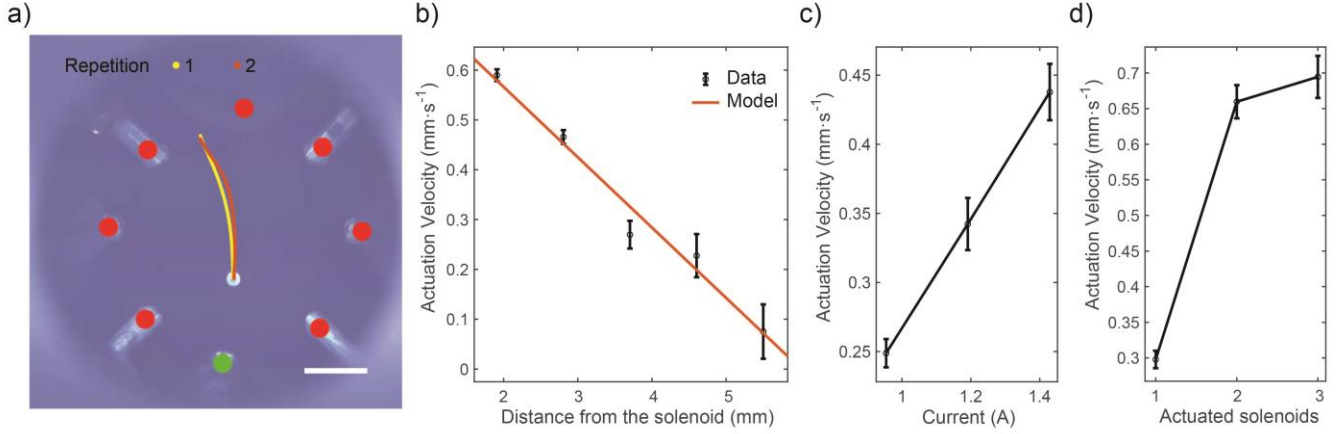


Fig. 5. Open-loop performance the ferrofluid manipulator a) A polyethylene (PE) particle motion induced by a single solenoid b) Actuation velocity of the PE particle placed at different initial distances from the actuated solenoid c) Actuation velocity of the PE particle when a solenoid is actuated with different currents. d) Actuation velocity of the PE particle when a different number of solenoids are actuated simultaneously. The scale bar is 2 mm.

proportional dependency can be linearly described as $v_a = -0.14\rho + 0.85$, where v_a is the actuation velocity of the particle, in mm/s, and ρ is the distance from the particle to the solenoid, in mm. Note, the relationship is valid only for distance up to ~ 6 mm. The standard deviation of the actuation velocity of the particle is smaller when the initial position is nearer the solenoid, and greater when the initial position is further away from the solenoid.

The influence from the actuation current to the actuation velocity of the particle is studied by repeating the pushing experiments at the same initial position of 2.56 mm at three current values of 0.95 A, 1.19 A, and 1.43 A. The experiment was repeated five times for each current value. Since the drift of the PE particles on the air-ferrofluid interface become

significant compared to the pushing motion of the ferrofluid when the actuation current of the solenoid is below 0.95 A, the experiments were carried out for actuation current above 0.95 A. Fig. 6 c. shows that the actuation velocity of the particles is linear with respect to the current and can be described as $v_a = 0.40I - 0.13$, where I is the current. The standard deviation of the actuation velocity increases with the actuation current, attributed to the greater oscillation of the ferrofluidic bump caused by the greater step actuation current of the solenoid. Notice that the relationship between the actuation velocity and the actuation current is valid only above 0.47 A.

To study the actuation ability of multiple solenoids, we measured the particle actuation velocity when actuated by one, or simultaneously two, or three solenoids with the initial particle position at the center of the workspace, i.e., ~ 3.9 mm from the solenoid. The results (Fig. 6 d) show that the actuation velocity of a particle for one actuated solenoid was 0.30 ± 0.01 mm/s and for two solenoids was 0.66 ± 0.02 mm/s, representing an increase of 121.5%. However, when the actuation was performed with three solenoids, the increase was only 5.3% to 0.69 ± 0.03 mm/s. See the Supplementary multimedia file for videos.

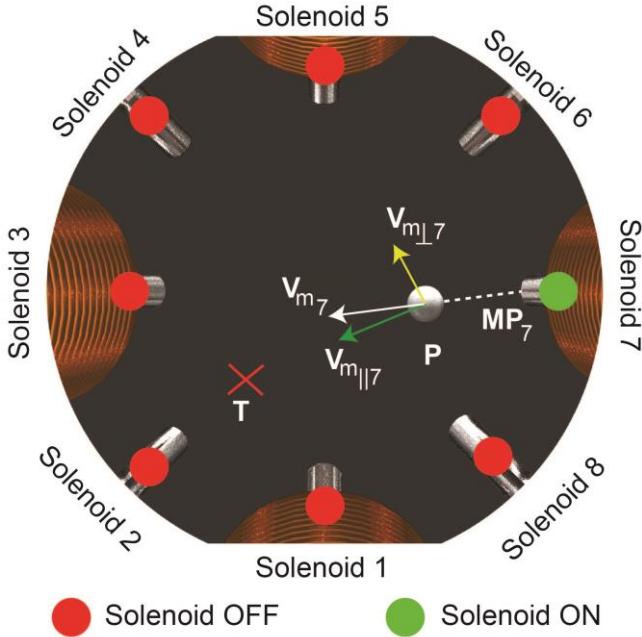


Fig. 6. Illustration of the path-following control algorithm. A particle P in the workspace is defined with its position coordinates (x_p, y_p) and a target $T(x_t, y_t)$ in respect to the origin O (upper-left corner of the frame). The particle moves with \vec{V}_{m7} since solenoid 7 is ON. $V_{m||7}$ and $V_{m\perp7}$ are parallel and orthogonal projections of \vec{V}_{m7} respectively. The particle is at a distance MP_7 from the solenoid 7.

V. AUTOMATIC PATH-FOLLOWING CONTROL

To achieve automatic path-following of the particles, we use a linear programming based visual servoing control algorithm. The inputs to the algorithm are the current position $P(x_p, y_p)$ of the particle and the target location $T(x_t, y_t)$ as illustrated in Fig. 6. Both, P and T , are defined in respect to the origin $O(0, 0)$, which is in the upper left corner of the frame, not shown in the figure. The current position of the particle is identified by performing grey-level thresholding [28] and blob detection on the images captured by the camera. The output of the algorithm S , is a 1×8 array of zeros and ones, where a zero denotes the OFF state and a 1 denotes the ON state of a solenoid. The force calculation of the particle derived from equation (1) can be only numerically solved. On the other hand, the actuation velocity of the particle with respect to the distance from the solenoid is linear as indicated in Figure 5b. Therefore, in real-time

trajectory and positioning control, we can estimate the expected motion of the particle using the understanding of the actuation velocity obtained in the previous section. Specifically:

$$\vec{V}_{m_{i=1..8}} = (-a\|\overline{MP}\|_i + b) \cdot \frac{\overline{MP}_i}{\|\overline{MP}\|_i} \quad (3)$$

where $\vec{V}_{m_{i=1..8}}$ are expected velocity projections on the particle, $a = -0.14$, $b = 1.0$ and \overline{MP}_i are the displacement vectors from each solenoid to the micro-object, $\|\cdot\|$ is the vector norm operator.

The scalar projections of \vec{V}_m parallel and orthogonal to \overline{PT} is denoted by $V_{m\parallel i=1..8}$ and $V_{m\perp i=1..8}$ respectively. This scalar projection can be expressed as the following dot products:

$$V_{m\parallel i=1..8} = \vec{V}_{m_{i=1..8}} \cdot \frac{\overline{PT}}{\|\overline{PT}\|}, V_{m\perp i=1..8} = \vec{V}_{m_{i=1..8}} \cdot \frac{\overline{PT}_\perp}{\|\overline{PT}_\perp\|} \quad (4)$$

where \overline{PT}_\perp is the orthogonal vector of \overline{PT} .

The main objective of the control algorithm is to reach the particle to the target by maximizing the motion along \overline{PT} and minimizing the motion along \overline{PT}_\perp without any limitation of simultaneous actuation of multiple solenoids. This objective is a multi-objective optimization problem whose cost function J can be represented as:

$$J = \sum_{i=1}^8 \alpha(V_{m\parallel i} S_i) - \beta(|V_{m\perp i}| S_i) - \gamma \left(\frac{1}{\|\overline{PT}\|^2} S_i \right) \quad (5)$$

where $|\cdot|$ is the absolute-value norm. The last term in the cost function is distance-dependent between the particle and the target $\|\overline{PT}\|$, so that number of actuated solenoids are reduced when the particle is closer to the target and vice versa. The parameters α , β , γ were experimentally tuned such that $\alpha = 0.4145$, $\beta = 0.2685$ and $\gamma = 0.0001$.

The cost function was solved using the mixed-integer linear programming method (MILP) [29] and a weighted sum approach, which was implemented using CPLEX 12.10 library. Image processing algorithms were developed using ViSP (Visual Servoing Platform) library [30].

TABLE II. PATH FOLLOWING ERRORS

Path	Mean Error (μm)	Standard Deviation ($\mu\text{m/s}$)	Max Error (μm)
Line	57.4	33.6	162
Square	74	44.4	322
Circle	67.2	38.6	236.4

TABLE III. VELOCITY DURING PATH FOLLOWING

Path	Mean Velocity ($\mu\text{m/s}$)	Standard Deviation ($\mu\text{m/s}$)	Max Velocity ($\mu\text{m/s}$)
Line	349.2	64.8	508.2
Square	357.1	33.5	416.1
Circle	443.4	21.5	475.9

The performance of the control method was evaluated with line, square and circular path-following repeatability tests using a PE particle as shown in Fig.7, and see the Supplementary multimedia file for videos. All solenoids were excited with constant voltage of 6 V and corresponding current of about 1.4 A. The trajectories were repeated ten times where only three repetitions are shown in Fig. 7 for clarity. The particle was moved from left to right following a 3 mm line where the origin of the plot is at the center of the workspace. The relative greater deviation from the reference trajectory at the starting position can be attributed to the step actuation of the ferrofluid. At the end of the trajectory, the deviation is also greater due to the greater distance between the particle to the solenoids in actuation (see Fig. 5b).

Table II summarizes the path following errors for all three paths. Similar to the line path, greater deviation of the square path also occurs at the starting position due to step actuation, and the increased distance from the actuation solenoids to the particle. However, the square path also involves the particle motion in off-center path, where the distance to actuation solenoids is asymmetric, resulting to greater standard deviation and maximum error.

Table III summarizes the resultant velocities when manipulating the particle in the reference trajectories. For the line following, the average velocity is lowest, but the maximum

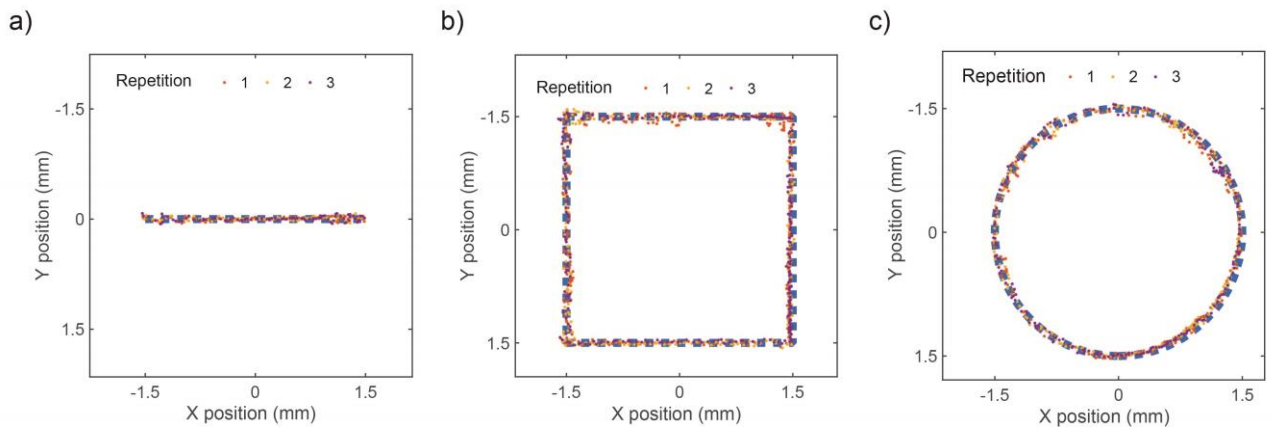


Fig 7. Automatic path-following control of a PE particle for reference paths of a) line b) square, and c) circle. The blue dashed line is the reference trajectory.

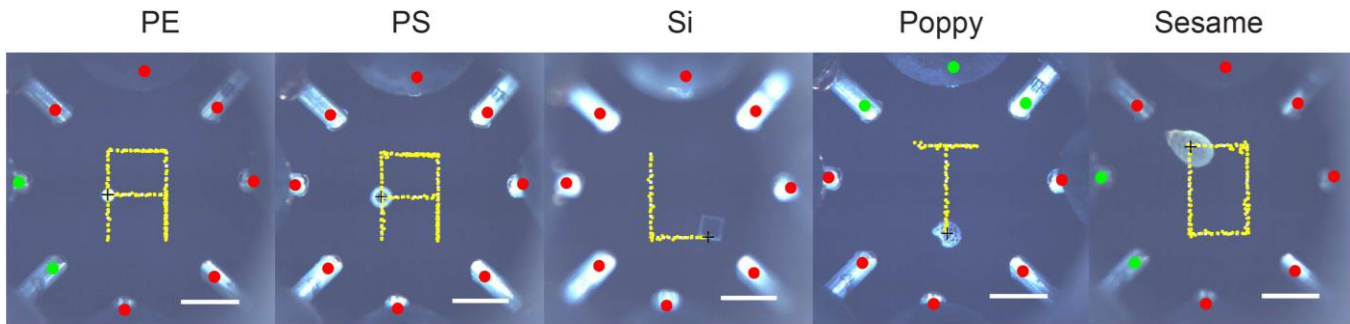


Fig 8. Automatic path-following manipulation of a polyethylene (PE) and a polystyrene (PS) particles, a silicon (Si) chip; a poppy seed and sesame in writing the letters “AALTO”. The trajectory (in yellow) is down sampled three times. The scale bar is 2 mm.

velocity is highest. The reason is that the motion is induced only by the solenoids on the left side (solenoid 2, 3 and 4), which was initially very effective but weakens with the increasing distance between the actuated solenoids and the particle, especially at the end of the trajectory. On the other hand, average velocity for circular path following is the highest, since the average distances between the actuated solenoid and the particle are relatively closer along the path. A greater deviation from the reference paths in the case of square and circular trajectories were also observed at the top side near solenoid 4, 5 and 6. These deviations can be attributed to the differences among the solenoids.

Figure 8 shows the manipulation of different types of objects in writing the letters “AALTO”. A PE particle and a PS particle were manipulated in writing the letter “A”. A silicon chip was manipulated in writing the letter “L”. A poppy and a sesame seed were manipulated in writing the letters “T” and “O”. The proposed algorithm is adaptable in manipulating objects of different materials, shapes, and sizes merely by altering the supply voltage/current. The polyethylene (PE) spherical particle was manipulated with 6 V supply voltage, translating to ~ 1.4 A in current. The polystyrene (PS) spherical particle was manipulated with 5 V, or ~ 1.2 A. The silicon chip is manipulated with 2 V, or ~ 0.47 A. The poppy and sesame seeds are manipulated with 4 V and 3 V, or 0.95 and 0.7 A, respectively. See the Supplementary multimedia file for videos.

VI. SUMMARY AND DISCUSSION

This paper reported a ferrofluid manipulator that can automatically manipulate floating non-magnetic micro-objects by deforming the interface of a ferrofluid using eight centimeter-scale solenoids. Employing a linear programming-based control algorithm, the manipulator can control the motion of non-magnetic particles following different paths, from line, circle, square to different letter-like trajectories. The achieved path following precision is as good as $57 \mu\text{m}$ for a 0.5 mm PE particle. For achieving more precise path-following control, a pulse-width modulation (PWM) or current control circuits for each solenoid could be constructed.

The manipulator is also versatile. Despite the simplicity of the path following control algorithm, the manipulator can manipulate non-magnetic particles of different materials and of different shapes, including spherical polyethylene (PE) and polystyrene (PS) particles, a square silicon (Si) chip, and natural shaped poppy and sesame seeds.

As a future work, the proposed technique could be extended to using biocompatible ferrofluids [31] for the manipulation of cellular cultures on the air-ferrofluid interface. Some potential modifications employing electromagnetic needles [9] [10] could also be considered to concentrate the magnetic field for manipulating smaller objects as well as to decrease the impact of possible geometrical constraints. Another direction that could be explored is on manipulation of multiple objects on the ferrofluidic interface by employing machine learning based approaches.

ACKNOWLEDGMENT

The authors would also like to express their gratitude to Heikki Hyyti, Vesa Korhonen, and Visa Lukkarinen for support in the design and the manufacture of the custom-made electronic board. Z.C. acknowledges the incentive stipend provided by Neles Foundation.

REFERENCES

- [1] M. P. Kummer *et al.*, “Magnetic Mediated Hyperthermia: Current Status and Future Directions,” *Int. J.*, vol. 26, no. 4, p. 1972, 2010, doi: 10.1080/0265673011010878.
- [2] O. Felfoul *et al.*, “Magneto-aerotactic bacteria deliver drug-containing nanoliposomes to tumour hypoxic regions,” *Nat. Nanotechnol.*, vol. 11, no. 11, pp. 941–947, 2016, doi: 10.1038/nnano.2016.137.
- [3] X. Wang *et al.*, “NANOROBOTS: Intracellular manipulation and measurement with multipole magnetic tweezers,” *Sci. Robot.*, 2019, doi: 10.1126/scirobotics.aav6180.
- [4] A. Menciassi, M. Quirini, and P. Dario, “Microrobotics for future gastrointestinal endoscopy,” *Minim. Invasive Ther. Allied Technol.*, vol. 16, no. 2, pp. 91–100, 2007, doi: 10.1080/13645700701266982.
- [5] B. J. Nelson, I. K. Kaliakatsos, and J. J. Abbott, “Microrobots for minimally invasive medicine,” *Annu. Rev. Biomed. Eng.*, vol. 12, pp. 55–85, 2010, doi: 10.1146/annurev-bioeng-010510-103409.
- [6] R. Bernasconi *et al.*, “Magnetically navigable 3D printed multifunctional microdevices for environmental applications,” *Addit. Manuf.*, vol. 28, no. April, pp. 127–135, 2019, doi: 10.1016/j.addma.2019.04.022.
- [7] M. Salehzadeh and E. Diller, “Two-agent formation control of magnetic microrobots in two dimensions,” *J. Micro-Bio Robot.*, vol. 12, no. 1–4, pp. 9–19, 2017, doi: 10.1007/s12213-017-0095-5.
- [8] E. Diller, J. Giltinan, and M. Sitti, “Independent control of multiple magnetic microrobots in three dimensions,” *Int. J. Rob. Res.*, vol. 32, no. 5, pp. 614–631, 2013, doi: 10.1177/0278364913483183.
- [9] Z. Cenev *et al.*, “Manipulating Superparamagnetic Microparticles with an Electromagnetic Needle,” *Adv. Mater. Technol.*, vol. 3, no. 1, 2018, doi: 10.1002/admt.201700177.
- [10] J. Seon, Z. Cenev, and Q. Zhou, “Automatic Non-Contact Extraction

- and Independent Manipulation of Magnetic Particles Using Electromagnetic Needle,” vol. 4435, no. c, 2019, doi: 10.1109/TMECH.2019.2960860.
- [11] J. Yu, B. Wang, X. Du, Q. Wang, and L. Zhang, “Ultra-extensible ribbon-like magnetic microswarm,” *Nat. Commun.*, vol. 9, no. 1, p. 3260, Dec. 2018, doi: 10.1038/s41467-018-05749-6.
- [12] H. Xie *et al.*, “Reconfigurable magnetic microrobot swarm: Multimode transformation, locomotion, and manipulation,” *Sci. Robot.*, 2019, doi: 10.1126/scirobotics.aav8006.
- [13] F. Qiu, S. Fujita, R. Mhanna, L. Zhang, B. R. Simona, and B. J. Nelson, “Magnetic Helical Microswimmers Functionalized with Lipoplexes for Targeted Gene Delivery,” *Adv. Funct. Mater.*, vol. 25, no. 11, pp. 1666–1671, 2015, doi: 10.1002/adfm.201403891.
- [14] W. Hu, G. Z. Lum, M. Mastrangeli, and M. Sitti, “Small-scale soft-bodied robot with multimodal locomotion,” *Nature*, vol. 554, no. 7690, pp. 81–85, 2018, doi: 10.1038/nature25443.
- [15] M. S. Gabureac, L. Bernau, G. Boero, and I. Utke, “Single superparamagnetic bead detection and direct tracing of bead position using novel nanocomposite nano-hall sensors,” *IEEE Trans. Nanotechnol.*, vol. 12, no. 5, pp. 668–673, 2013, doi: 10.1109/TNANO.2013.2266733.
- [16] S. Schuerle *et al.*, “Robotically controlled microprey to resolve initial attack modes preceding phagocytosis,” *Sci. Robot.*, vol. 2, no. 2, p. eaah6094, Jan. 2017, doi: 10.1126/scirobotics.aah6094.
- [17] M. Dkhil, M. Kharboutly, A. Bolopion, S. Regnier, and M. Gauthier, “Closed-Loop Control of a Magnetic Particle at the Air-Liquid Interface,” *IEEE Trans. Autom. Sci. Eng.*, vol. 14, no. 3, pp. 1387–1399, 2017, doi: 10.1109/TASE.2015.2448133.
- [18] L. Yang, E. Yu, C. I. Vong, and L. Zhang, “Discrete-Time Optimal Control of Electromagnetic Coil Systems for Generation of Dynamic Magnetic Fields with High Accuracy,” *IEEE/ASME Trans. Mechatronics*, vol. 24, no. 3, pp. 1208–1219, 2019, doi: 10.1109/TMECH.2019.2907656.
- [19] B. V. Johnson, S. Chowdhury, and D. J. Cappelleri, “Local Magnetic Field Design and Characterization for Independent Closed-Loop Control of Multiple Mobile Microrobots,” *IEEE/ASME Trans. Mechatronics*, vol. 25, no. 2, pp. 526–534, 2020, doi: 10.1109/TMECH.2020.2969074.
- [20] M. Gauthier and E. Piat, “Control of a Particular Micro-Macro Positioning System Applied to Cell Micromanipulation,” *IEEE Trans. Autom. Sci. Eng.*, vol. 3, no. 3, pp. 264–271, 2006, doi: 10.1109/TASE.2005.861398.
- [21] M. S. Sakar, E. B. Steager, D. H. Kim, M. J. Kim, G. J. Pappas, and V. Kumar, “Single cell manipulation using ferromagnetic composite microtransporters,” *Appl. Phys. Lett.*, vol. 96, no. 4, pp. 2010–2013, 2010, doi: 10.1063/1.3293457.
- [22] E. Diller and M. Sitti, “Three-dimensional programmable assembly by untethered magnetic robotic micro-grippers,” *Adv. Funct. Mater.*, vol. 24, no. 28, pp. 4397–4404, 2014, doi: 10.1002/adfm.201400275.
- [23] E. Diller, Z. Ye, and M. Sitti, “Rotating magnetic micro-robots for versatile non-contact fluidic manipulation of micro-objects,” pp. 1291–1296, 2011, doi: 10.1109/iros.2011.6094968.
- [24] X. Yang *et al.*, “An agglutinate magnetic spray transforms inanimate objects into millirobots for biomedical applications,” *Sci. Robot.*, vol. 5, no. 48, pp. 1–13, 2020, doi: 10.1126/scirobotics.abc8191.
- [25] R. Ahmed, M. Ilami, J. Bant, B. Beigzadeh, and H. Marvi, “A Shapeshifting Ferrofluidic Robot,” *Soft Robot.*, vol. 00, no. 00, pp. 1–12, 2020, doi: 10.1089/soro.2019.0184.
- [26] X. Fan, X. Dong, A. C. Karacakol, H. Xie, and M. Sitti, “Reconfigurable multifunctional ferrofluid droplet robots,” *Proc. Natl. Acad. Sci. U. S. A.*, vol. 117, no. 45, pp. 27916–27926, 2020, doi: 10.1073/pnas.2016388117.
- [27] Z. Cenev, A. Würger, and Q. Zhou, “Main Manuscript for Motion and Trapping of Micro- and Millimeter Spheroid Particles on the Air-Paramagnetic Liquid Interface,” 2020.
- [28] N. Otsu, “Threshold Selection Method From Gray-Level Histograms,” *IEEE Trans Syst Man Cybern.*, vol. SMC-9, no. 1, pp. 62–66, 1979, doi: 10.1109/TSMC.1979.4310076.
- [29] A. Schrijver, *Theory of linear and integer programming*. John Wiley & Sons, 1998.
- [30] É. Marchand, F. Spindler, and F. Chaumette, “ViSP: A generic software platform for visual servoing,” *IEEE Robot. Autom. Mag.*, vol. 12, no. November 2011, pp. 40–52, 2005.
- [31] J. V. I. Timonen, C. Raimondo, D. Pilans, P. P. Pillai, and B. A. Grzybowski, “Trapping, manipulation, and crystallization of live cells using magnetofluidic tweezers,” *Nanoscale Horizons*, vol. 2, no. 1, pp. 50–54, 2017, doi: 10.1039/c6nh00104a.